DOI: 10.13009/EUCASS2023-922
Aerospace Europe Conference 2023 – 10TH EUCASS – 9TH CEAS

Comparison of Experimental Fatigue Life Study for two Inner Liner Materials for Liquid Rocket Engines

Pascal H. Kringe[1,4], *Jörg R. Riccius*[1], *Justin Hardi*[1], *Michael Oschwald*[1,2], *Stefanie Reese*[3]
[1] *German Aerospace Center (DLR), Institute of Space Propulsion, 74239 Lampoldshausen, Germany*
[2] *RWTH Aachen University, Institute of Jet Propulsion and Turbomachinery, Aachen, Germany*
[3] *Institute of Applied Mechanics, RWTH Aachen University, Aachen, Germany*
[4] Corresponding author: pascal.kringe@dlr.de

Abstract

The paper on hand presents the comparison of two experimental fatigue life studies conducted with two copper alloys. The alloys are Cu-HCP and CuCrZr. Both materials can be used as the inner liner material for regeneratively cooled liquid rocket engines. The experimental aspect of this study uses Thermomechanical Fatigue (TMF) panels. A TMF panel represents a small section of a regeneratively cooled rocket combustion chamber. It typically contains 7 cooling channels. The coolant being used is supercritical nitrogen instead of hydrogen or methane due to safety and cost concerns. The TMF test bench also incorporates a high power diode laser radiating onto the TMF panel surface. This provides realistic amounts of heat flux and surface temperature. The laser is cyclically powered on and off to represent the multiple load cycles that liquid rocket engines have to endure particularly in reusable rocket engines. This procedure is repeated until the central cooling channel cracks. The setup of the TMF test bench provides data regarding the pure mechanical performance of the material without the influences of any combustion or chemical effects. Furthermore, heat flux, surface temperature and mass flow rate can be determined easily, hence providing precise input data for numerical simulations and validation. The test conditions of both TMF panel test campaigns were a heat flux of $\dot{q} = 24.25\ \mathrm{MW/m^2}$ and a maximum surface temperature of $T_s = 800$ K. Data obtained in the test campaigns comprise fluid properties, temperature distribution as well as mechanical behavior like displacement and strain on the laser loaded surface. The difference in the amount of laser power cycles defines the fatigue life behavior.

1. Introduction

In today's space launch systems, regeneratively cooled liquid rocket engines (LRE) are state of the art. Within the engine assembly, the combustion chamber inner liner is one of the most critical parts. In particular, regeneratively cooled combustion chambers have to withstand high temperatures, extreme temperature gradients and large pressure differences. These aspects become especially important when it comes to the reusability of launcher systems as current trending on the launcher market suggests. The multiple cyclic operation of reusable liquid rocket engines causes thermomechanical fatigue (TMF). TMF consists mainly of effects such as the accumulation of plastic strains, creep deformation and thermal ageing. As the majority of engine development is conducted using numerical methods such as finite element analysis (FEA) and computational fluid dynamics (CFD) there is a growing demand for validated simulation methods. For this purpose, the TMF panel test bench was developed at DLR's Institute of Space Propulsion.[3,8,13,16] Both, the TMF panel and the test bench are capable of producing high quality experimental data that is used to validate simulations. A TMF panel typically consists of 7 cooling channels of which the 5 innermost have a similar geometry to a LRE combustion chamber wall. For safety and cost reasons the TMF panel is cooled with supercritical nitrogen and heated by a high power diode laser system providing high amounts of heat flux. The TMF panel is cyclically heated by the laser until a crack in the central cooling channel occurs. Similar research into low cycle fatigue using TMF panels dates back to Carden[2] in 1966 and Quentmeyer in 1977.[11] Riccius,[13] Gernoth[4] and Thiede[17] published the first results of the TMF test bench at DLR from 2007 onward. Kringe continued the work[9] with a focus on the heat flux properties[6] and fatigue life.[7] Hötte[5] also conducted fatigue life experiments using TMF panels made of CuCr1Zr. The manuscript on hand compares the experimental results of two TMF panels tested at the test bench at DLR Lampoldshausen. The first TMF panel was made of Cu-HCP, the second alloy was CuCrZr. Both TMF panel test campaigns had the same boundary conditions i.e. geometry, surface temperature and fluid temperature and pressure at the begin of a cycle. The experimental data presented here relate to a surface temperature of $T_s = 800$ Kand a heat

DOI: 10.13009/EUCASS2023-922

flux of $\dot{q}$ = 24.25 MW/m^2. A comparison of the different fatigue life performance and fluid properties of the nitrogen coolant is presented. Furthermore, the thermal field on the laser heated surface is compared as well as the deformation during the course of the test. Finally, a CT scan of the different damage behavior is given to evaluate the internal shape of the TMF panel.

2. Test Setup

This section gives a brief overview of the experimental setup, which includes the TMF panel itself, the M51 test bench at DLR's Lampoldshausen Institute of Space Propulsion and the applied test conditions. A more detailed description can be found in earlier publications by Kringe.[7–9]

2.1 Thermomechanical Fatigue Panel

The TMF panel has been developed by Thiede.[16] It is the 3rd generation of TMF panels being assessed at DLR. Thiede also investigated the panel numerically for a surface temperature of T_s = 1000 K and $\dot{q}$ = 20 MW/m^2. The TMF panel consists of 7 cooling channels (see Fig. 1 and Fig. 4). Cooling channels 2 - 6 represent the actual geometry of a

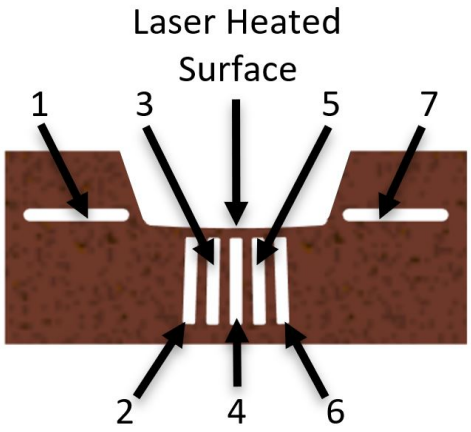

Figure 1: **Cross section of the TMF panel with cooling channels 1 (left) to 7 (right).**

regeneratively cooled LRE cooling channel. Channels 1 and 7 have a slightly increased cross section to effectively cool down the outer parts of the TMF panel. The cooled outer material induces a stress which is comparable to the hoop stress during shutdown of a LRE induced by the Nickel jacket that is typically galvanized onto the inner liner. This outer layer stiffens the combustion chamber in order to forward the generated thrust of the engine to the actual rocket body. In the TMF panel only the central cooling channel 4 is considered as representative regarding the stress and strain fields in a LRE. The dimensions of the TMF panel are listed in Table 1. The material used for

Table 1: **Dimensions of the TMF panel**

Dimension	Value
Total size	48 × 230 × 20 mm
Number of cooling channels	5 + 2
Laser-heated wall thickness	1 mm
Channel width	1.3 mm
Fillet width	1.0 mm
Height of channels 2 - 6	9 mm
Corner Radius	0.24 mm
Angular separation	1°
Laser loaded surface	cylindrical r = 130 mm

DOI: 10.13009/EUCASS2023-922

the TMF panels is Cu-HCP (high-conductivity copper) and CuCrZr (Copper-Chromium-Zirconium), respectively. The relevant thermophysical parameters are presented in Figure 2. Herein λ is the thermal conductivity, c_p describes the

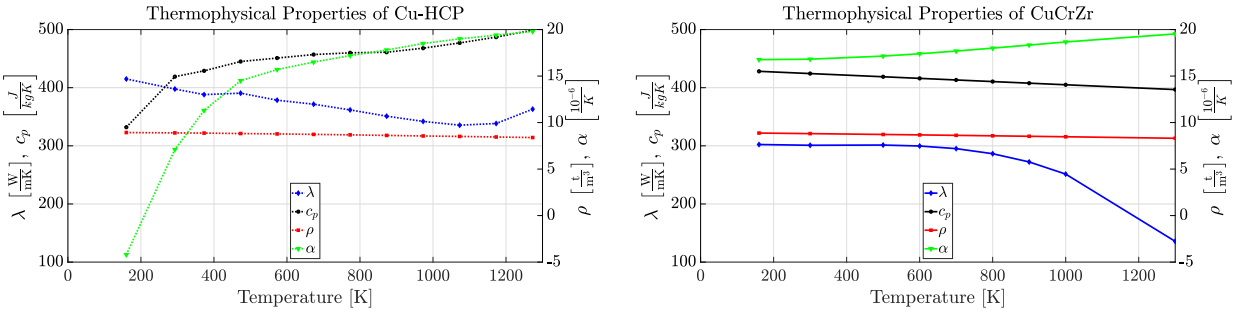

(a) Cu-HCP (b) CuCrZr

Figure 2: **Thermophysical Properties of the two different alloys.**

heat capacity, ρ is the density and α denotes the coefficient of thermal expansion. The thermophysical properties of CuCrZr are taken from Thiede,[16] whilst the thermophysical properties of Cu-HCP were experimentally determined by Fraunhofer IWM[6,14] and taken from Oschwald[10] for cryogenic temperatures, respectively. It is obvious, that CuCrZr has a lower ($\approx 20\%$) heat conductivity λ but a slightly higher ($\approx 5\%$) coefficient of thermal expansion α at $T = 800$ K. However, for Cu-HCP the coefficient of thermal expansion decreases significantly for lower temperatures, whilst it is rather constant for CuCrZr. This is one important difference in both materials regarding the fatigue life behavior. Due to the very low emissivity of copper,[1,18] oxidized copper and also CuCrZr at the wavelength of the laser (see Tab. 2) the TMF panel is coated to increase its emissivity to $\varepsilon_{940\ \mathrm{nm}} = 0.95$ at a surface temperature around $T_\mathrm{s} = 800$ K.

2.2 TMF Panel Test Bench

The TMF panel test bench at DLR Lampoldshausen was built in 2006 - 2007 by Gernoth[4] and Riccius.[13] It consists of three main components: the fluid system, the control and measurement system and the test cell which contains the high power diode laser and test specimen. They are introduced briefly in this section. For more details see Kringe,[8] Thiede[16] and Gernoth.[3]

2.2.1 High Power Diode Laser System

The throat section of liquid rocket engines endures heat fluxes of exceptionally high values ranging from $\dot{q}_\mathrm{w} = 80$ MW/m^2 (Vulcain) to $\dot{q}_\mathrm{w} = 120$ MW/m^2 (RS-25).[15] Only high power diode laser systems allow testing the TMF panels under laboratory conditions at near representative heat loads. Two main advantages of this system compared to combustion or other heating devices is the safe operation of the laser and the precise control of the heat flux. Additionally, it allows for the exclusive study of the purely mechanical and thermal performance of the TMF panel geometry and the material making the tests easily comparable. Effects such as hydrogen embrittlement, abrasion, blanching or combustion instabilities that might occur in conjunction with combustion are excluded, however, they have to be taken into account when investigating real LREs.[12] The laser used in the TMF Panel Test bench was manufactured by DILAS. It has a top hat shaped focal plane of $A_\mathrm{L} = 11.2$ mm $\times$ 32.2 mm to provide a dedicated area of constant heating (not a punctual hot spot or Gaussian intensity distribution). The technical data of the laser itself is listed in Table 2. A view of the

Table 2: **Technical parameters of the DILAS diode laser**

Parameter	Symb.	Value
Laser wavelength	λ	940 ± 10 nm
Optical power output	P	11 kW
Focal plane size	A	11.2 mm × 32.2 mm
Focal distance	l	399 mm
Homogeneity		< ±5 %
Max. output intensity	I	28 MW/m^2

DOI: 10.13009/EUCASS2023-922

distribution of the top hat intensity is presented in Figure 3. The output power P_{out} of the laser is linearly linked to an

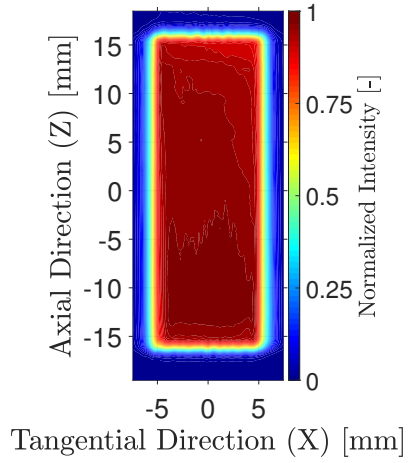

Figure 3: **Normalized laser top hat intensity in the focal plane at U_{ctrl} = 5.7 V**

output control voltage U_{ctrl} of the measurement and control system represented by Equation (1)

$$P_{\text{out}} = 2120.4 \frac{\text{W}}{\text{V}} U_{\text{ctrl}} - 2438.6\text{W}. \tag{1}$$

Hence, the heat flux $\dot{q}_{\text{w}}$ into the TMF panel laser loaded area can be calculated directly by taking into account the area of nearly constant (±2.5%) intensity in the top hat region and the emissivity leading to Equation (2)

$$\dot{q}_{\text{w}} = 5.454 \frac{\text{MW}}{\text{m}^2\text{V}} U_{\text{ctrl}} - 6.834 \frac{\text{MW}}{\text{m}^2}. \tag{2}$$

Note that Equations (1) and (2) were slightly changed compared to former work[6] because of maintenance and repair. However, the laser top hat profile and intensity distribution did not change measurably. The measurement uncertainty of the heat flux ranges between ±8.9% to ±13.5% depending on the surface temperature. This is caused by the uncertainty of both, the emissivity $\varepsilon_{940\text{ nm}}$ and the laser output power P_{out} (determined by a Primes Power meter (±2%)). That said, the reproducibility of the measurements is still in the order of ±1%. Additionally, the results presented in by Kringe,[6] i.e. the congruence of experimental and numerical data, indicate a much smaller uncertainty of the heat flux. Though, the precise quantification of the measurement uncertainty remains difficult.

2.2.2 Measurement and Control System

For accurate data recording the TMF panel is equipped with temperature sensors (thermocouples of Type K, accuracy ±0.4% of the measured value) at the inlet and outlet of each cooling channel to measure the fluid temperatures. Additionally, eight absolute pressure sensors (accuracy ±0.1% full scale) are installed to measure the pressure of the nitrogen coolant. Though, only one absolute pressure sensor is located at the inlet of the central cooling channel 4, the conditions herein are expected to be applicable to cooling channels 1-3 and 5-7 as well. The remaining pressure sensors are installed at the outlet of each cooling channel since the pressure values here differ due to the complex temperature field and convective heat transport resulting from the energy applied by the laser. Additionally, differential pressure sensors (accuracy ±0.25% full scale) are installed for each cooling channel, measuring the pressure drop over the heated area. All sensor locations are presented in Figure 4. The mass flow rate in each cooling channel is precisely controlled by seven control valves. Downstream of the valves, the individual mass flow rate is measured by Emerson Coriolis flow meter (accuracy ±0.1% of the measured value). The 2-dimensional temperature at the laser loaded surface is determined with a FLIR SC7600 infrared (IR) camera. The wavelength for the measurement is $\lambda_{\text{IR}} = 3.99\ \mu$m (accuracy ±1% or ±1 K). The deformation of the TMF panel surface is recorded during the progress of the test campaign via a digital image correlation (DIC) system from LIMESS GmbH. Two stereo cameras with a resolution of 16 megapixel are set up to take images with a frequency of up to 4 Hz. The 3 displacement components (u_{x}, $u_{\text{y}}, u_{\text{z}}$) can then be determined. The accuracy of the LIMESS measurement system depends on multiple parameters such as goodness of calibration and size of speckle marks. Therefore is can not generally be stated. Note that the DIC calculates the displacements and strains to a reference plane. For post test analysis a Keyence VHX-5000 microscope is available to determine the final shape of the laser loaded surface with high accuracy.

DOI: 10.13009/EUCASS2023-922

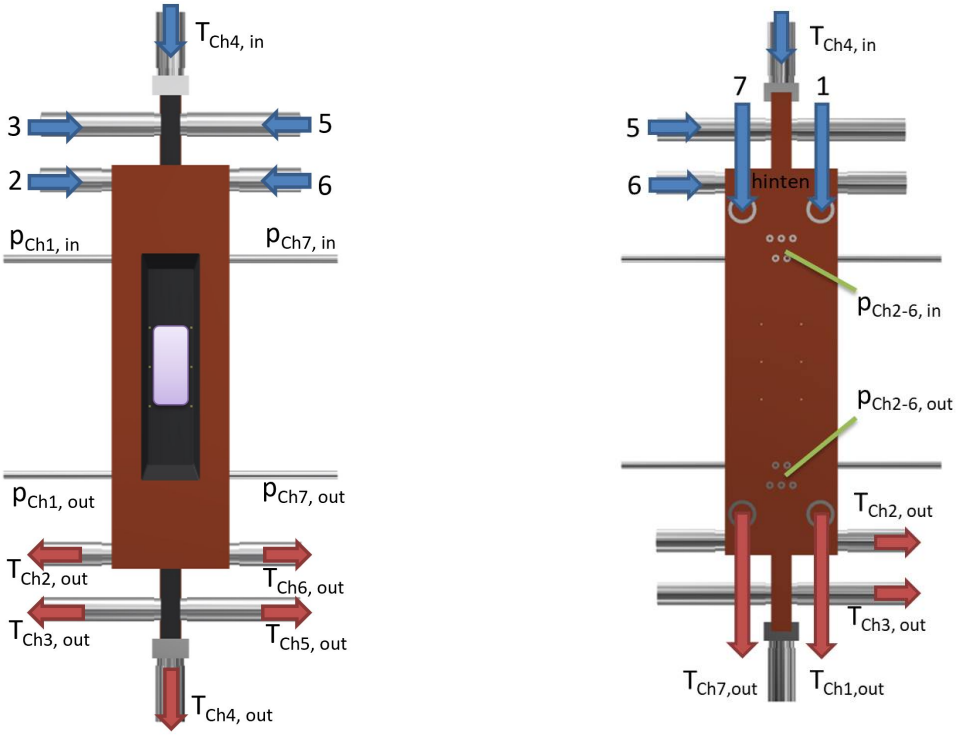

(a) Front side sensor locations

(b) Back side sensor locations

Figure 4: **Overview of sensor locations on the TMF panels**

2.2.3 Fluid System

The fluid system of the TMF Panel test bench provides the supercritical N_2 coolant for the TMF panel and dumps it into the environment after run through the test setup. The coolant consists of liquid nitrogen (LN_2, p = 5 bar, T = 94 K) supplied from a storage tank and pumped into the fluid system with a reciprocating piston pump, and gaseous nitrogen (GN_2, p = 150 bar, T = 288 K) provided by the supply loop installed on the DLR Lampoldshausen site infrastructure. Significant pressure drops are implemented to avoid oscillations from the feed system. After mixing, the N_2-coolant is then separated into the seven individual feed lines. The mass flow rates of the supply from the fluid system is ranging from $\dot{m}_{cc}$ = 8 g/s up to $\hat{\dot{m}}_{cc}$ = 50 g/s per cooling channel. Downstream of the panel the N_2 is merged within a collector before being dumped.

2.3 Test Conditions

To make TMF Panel tests comparable to each other, for each test campaign the fluid pressure at the outlet of cooling channel 4 is set to $p_{out} = 55 \pm 0.5$ bar and the fluid inlet temperature is fixed at $T_{in} = 160 \pm 2$ K at the time the laser is powered on. The pressure difference between the inside of the cooling channels and the environment in the test chamber is comparable to the pressure difference in a LRE. The fluid inlet temperature is fixed due to limitations of the test bench. With the above mentioned parameters being fixed the following parameters can be varied for detailed investigation of their influence on the fatigue life of the TMF panel. The test conditions used here are also noted in the following list:

1) Temperature of the laser loaded surface $T_s = 800 \pm 3$ K
2) Heat flux into the TMF panel $\dot{q}_w = 24.25$ MW/m^2 $\hat{=}$ $U_{ctrl} = 5.7$ V
3) Mass flow rate per cooling channel $\dot{m}_{cc,Cu-HCP} = 36.5 \pm 0.5$ g/s & $\dot{m}_{cc,CuCrZr} = 28.0 \pm 0.5$ g/s
4) Laser-on time $t_{on} = 200$ s

However, $\dot{m}_{cc}$, T_s and $\dot{q}_w$ are highly depending on each other. A detailed investigation of these dependencies for Cu-HCP was published by Kringe.[6] The experiment is set up in such way that the heat flux never exceeds $\dot{q}_w = 24.25$ MW/m^2, even if the surface temperature is not reached. In case the surface temperature is exceeded, the heat flux has to be reduced until the surface temperature is stable again at the desired value. To pursue a conservative approach and reach

DOI: 10.13009/EUCASS2023-922

the surface temperature from the beginning of the test campaign on, the mass flow rate for the first cycle was set 10% lower as calculated. Due to a known small asymmetry in the laser profile in the tangential direction (see Fig. 3) that yields a slightly asymmetric temperature profile, the mass flow in cooling channels 2 and 3 has been increased by $\Delta\dot{m}_{\mathrm{cc}} = +2$ g/s. The quantitative profile of the laser power output for a single cycle is presented in Figure 5. After the

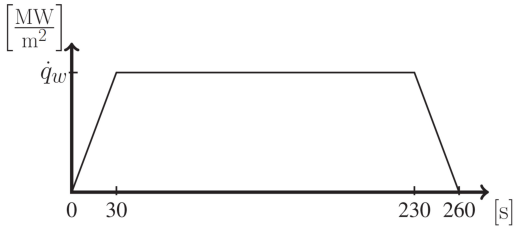

Figure 5: **Qualitative profile of the laser-on cycle consisting of linear ramp-up over 30 s, constant power and resulting constant heat flux for t_{on} = 200 s, and linear ramp-down over 30 s**

ramp-up, the surface temperature of the TMF panel is closely monitored by means of the IR camera. The power output is then adjusted if the surface temperature is not reached. Steady-state conditions are reached at around $t = 220$ s.

3. Results

This section presents and compares the experimental results of the two TMF panel tests for Cu-HCP and CuCrZr. It summarizes the fluid conditions in the representative central cooling channel 4 and the thermal behavior of the laser loaded surface as observed with the IR camera. Furthermore, the mechanical observations, i.e. the evolution of the strain of the laser loaded surface recorded with DIC and the internal deformation obtained by a CT-Scan are shown.
But first the most important results: The TMF panel made from Cu-HCP ruptured during the laser-on time of the **151st** cycle whilst the TMF panel made from CuCrZr ruptured during the ramp-down or post-cooling after the **645th** cycle. Note that throughout this manuscript the figures on the left side are referring to the Cu-HCP TMF panel test campaign, the figures on the right side refer to the CuCrZr TMF panel test campaign, respectively.

3.1 Coolant Conditions

The main fluid conditions in the course of both test campaigns are presented in Figures 6, 7 and 8. The dotted lines in the figures represent the conditions at the start of the cycle, i.e. when the laser is switched on ($t = 0$ s). They indicate that the predefined margins for $T_{4,\mathrm{in}}$ and $p_{4,\mathrm{out}}$ at the start of the laser could be met throughout the test campaigns. The solid lines represent the conditions at steady state ($t = 220$ s).
Figure 6 shows the different mass flow rates for the Cu-HCP (Fig. 6a) and CuCrZr (Fig. 6b). For the same heat flux and surface temperature CuCrZr needs approximately 25% less coolant than Cu-HCP. But this smaller mass flow rate leads to a higher outlet temperature at steady state conditions ($t_{\mathrm{on}} = 220$ s) of the coolant for CuCrZr than Cu-HCP as can be seen in Figure 7. For Cu-HCP the coolant outlet temperature rises by $\Delta T_{4,\mathrm{out}} \approx 22$ K (Fig. 7a) while for CuCrZr the increase is $\Delta T_{4,\mathrm{out}} \approx 27.5$ K (Fig. 7b). The same can be stated for the pressure in Figure 8. In the Cu-HCP TMF panel the absolute outlet pressure rises to $p_{4,\mathrm{out}} \approx 63$ bar (Fig. 8a) while in the CuCrZr TMF panel the pressure rises to $p_{4,\mathrm{out}} \approx 64$ bar (Fig. 8b). This is contradictory to the expectations. Because Cu-HCP has a higher thermal conductivity than CuCrZr as shown in Figure 2, the temperature at the fluid side should be higher for Cu-HCP according to Fourier's law

$$\dot{q}_\lambda = -\lambda(T)\,\nabla T. \tag{3}$$

Hence, a lower mass flow rate to transport the energy would be necessary as the convective heat flow rate depends on the difference between the wall temperature T_{w} and the bulk temperature of the fluid T_{b}

$$\dot{q}_{\mathrm{h}} = h(T_{\mathrm{w}} - T_{\mathrm{b}}). \tag{4}$$

The source of this discrepancy is not yet identified, though, two issues might contribute to this. First, the laser loaded surface of the Cu-HCP TMF panel has a roughness of $R_{\mathrm{a}} = 0.65$ μm, while for CuCrZr the roughness is $R_{\mathrm{a}} = 0.50$ μm. This probably changes the emissivity so less heat is applied to CuCrZr. Second, as can be seen in Figure 14a, the fillets of the Cu-HCP TMF panel show small marks from manufacturing. This might restrain the conductive heat flow to the lower parts of the cooling channel, prohibiting an efficient effect of the cooling fins. From Figure 6 another important aspect arises. While the mass flow rate for Cu-HCP has to be increased during the first half of the test campaign it later

DOI: 10.13009/EUCASS2023-922

has to be decreased even more to maintain the surface temperature of $T_s = 800$ K. Outlet temperature and pressure remain on a constant level. For CuCrZr this effect can not be observed, the mass flow rate rather has to be increased at the end of the fatigue life. For Cu-HCP it is assumed that three contrary effects cause the described pattern: thinning of the cooling channel wall and hence increase of the cooling channels cross-section due to deformation as well as degradation of the thermophysical parameters, in particular the heat conduction, due to material effects like aging or damage. The magnitude of each effect is difficult to predict and still under investigation.

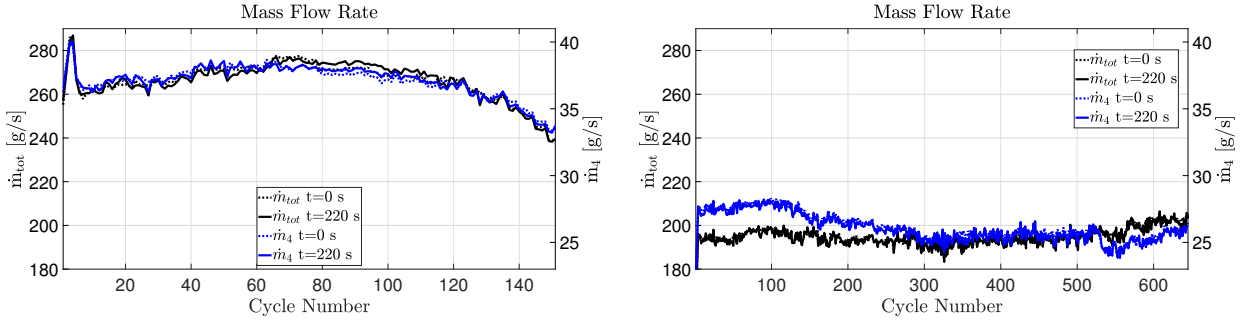

(a) Cu-HCP (b) CuCrZr

Figure 6: **Mass flow rate for all cycles.**

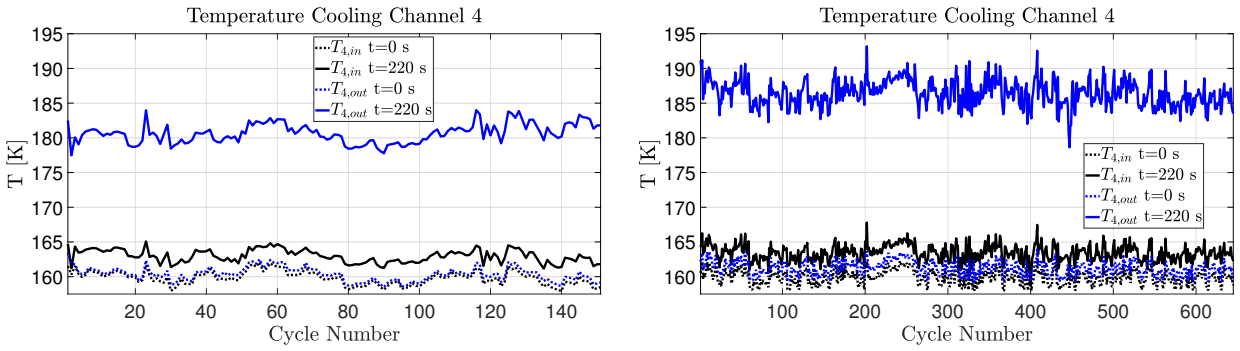

(a) Cu-HCP (b) CuCrZr

Figure 7: **Fluid temperature at inlet and outlet for all cycles.**

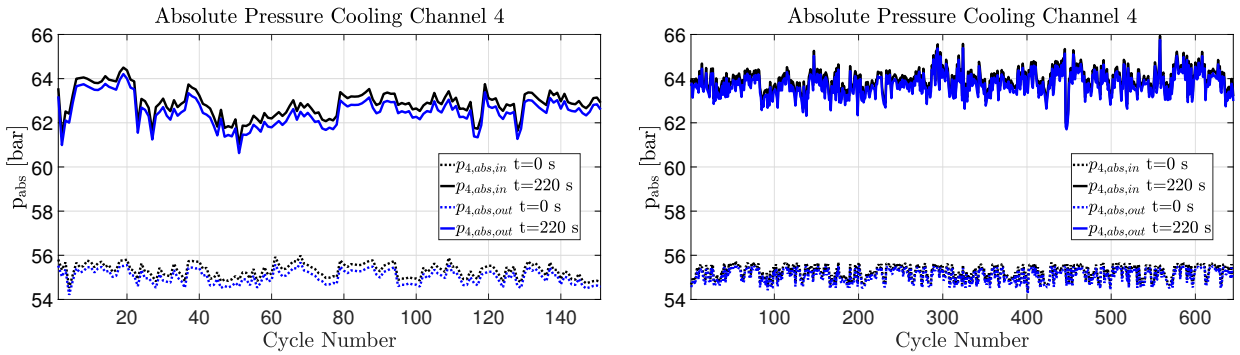

(a) Cu-HCP (b) CuCrZr

Figure 8: **Absolute pressure at inlet and outlet for all cycles.**

The balance of energy for both TMF panel test campaigns is presented in Figure 9. It is compound by the sum of all net heat flows, i.e. convective transfer into the coolant $\dot{Q}_h$, radiation from the laser $\dot{Q}_\varepsilon$ and conduction into the fluid supply system $\dot{Q}_\lambda$ as Equation (5) shows.

$$\sum \dot{Q}_\lambda + \sum \dot{Q}_\varepsilon + \sum \dot{Q}_h = 0 \tag{5}$$

DOI: 10.13009/EUCASS2023-922

In case of the TMF panel test, convection and radiation from and into the environment can be neglected. Figure 9 shows the normalized difference between the outlet heat flow rate $\dot{Q}_{\text{out}}$ comprised in the coolant due to convection which is calculated by the sum of enthalpy differences of all seven cooling channels

$$\dot{Q}_{\text{out}} = \sum_{i=1}^{7} \dot{m}_{\text{cc,i}} \left(h_{\text{out,i}} - h_{\text{in,i}} \right), \tag{6}$$

where h denotes the specific enthalpy, and the inward heat flow rate $\dot{Q}_{\text{in}}$ provided by the laser radiation.

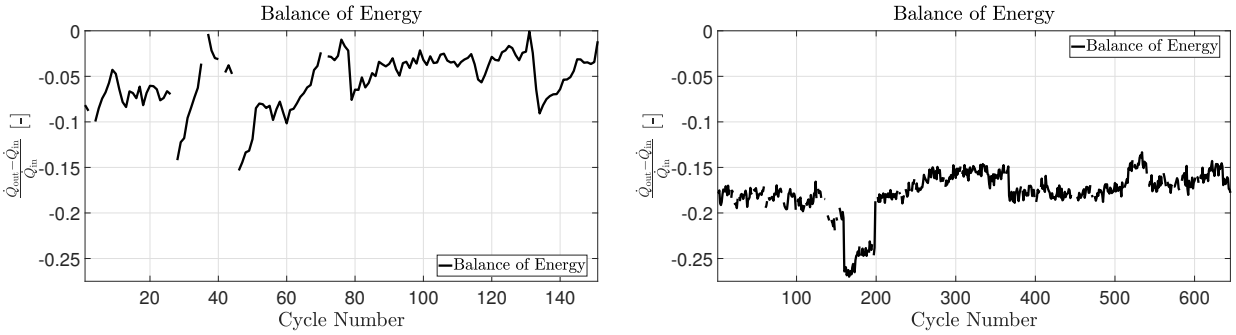

(a) Cu-HCP (b) CuCrZr

Figure 9: **Balance of energy for all cycles.**

3.2 Surface Thermal Field

Figures 10 and 11 show the comparison of the 2-dimensional temperature distribution on the laser heated surface for a cycle at the beginning of the test campaign, a cycle after half of the test campaign and at the last cycle before and after rupture. Note that the IR camera is only capable of measuring temperatures $T > 273$ K, hence, temperatures $T < 273$ K are indicated as $T = 0$ K. Also note, that, as mentioned before, the crack for Cu-HCP occurred during laser-on time, while for CuCrZr it occurred during ramp-down or the cool-down phase. Hence, Figure 11d was recorded after the cycle with very low laser power and a maximum temperature of $T = 308$ K to check if the TMF panel is already cracked. From Figures 10 and 11 one can see that the resolvable thermal field is slightly larger for CuCrZr. That is

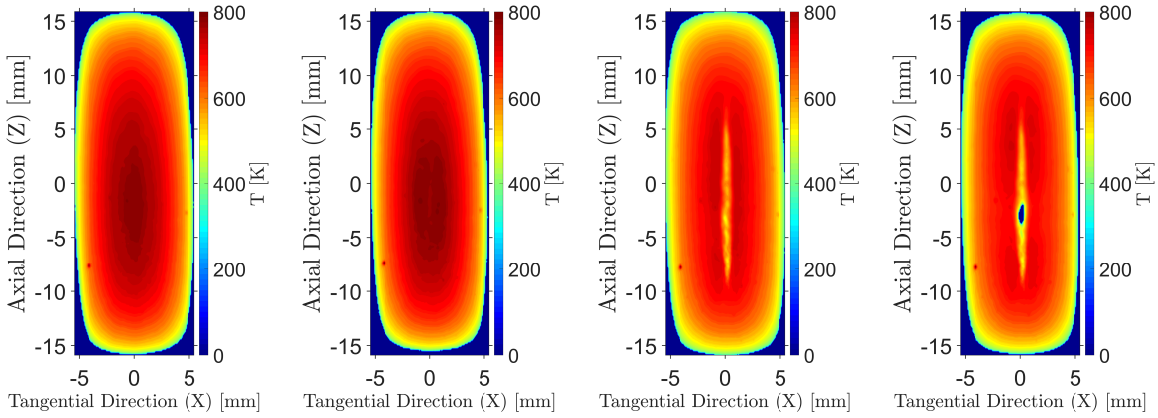

(a) Cycle 6 (b) Cycle 75 (c) Cycle 151 before crack (d) Cycle 151 after crack

Figure 10: **Temperature distribution of the laser loaded surface for Cu-HCP retrieved from the IR camera measurements for cycles 6, 75, and 151 directly before and after occurrence of the crack. Flow direction is top-down.**

referable to the lower thermal conductivity as seen in Figure 2. In the Cu-HCP test campaign the thermal field on the laser loaded surface already shows a small local line-shaped temperature minimum during laser-on cycle 75 (see Fig.

DOI: 10.13009/EUCASS2023-922

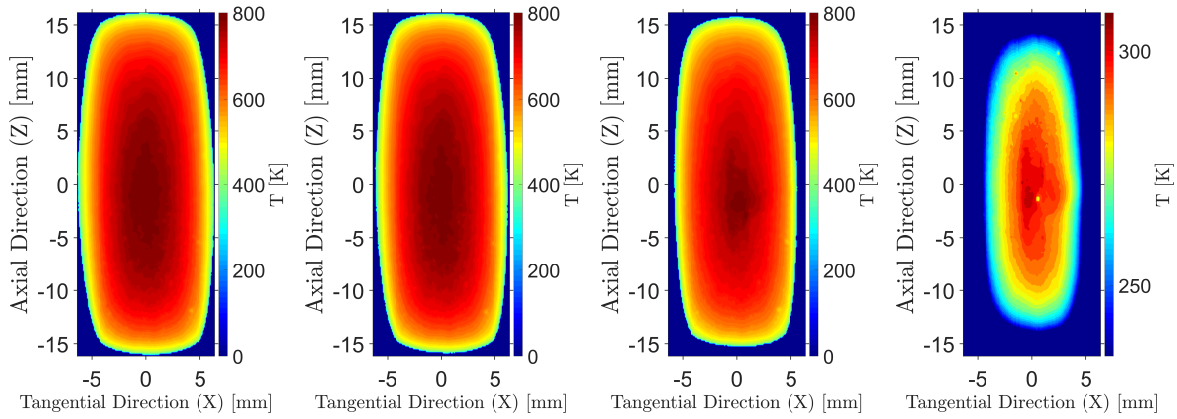

(a) Cycle 1 (b) Cycle 322 (c) Cycle 645 before crack (d) Cycle 645 after crack

Figure 11: **Temperature distribution on the laser loaded surface for CuCrZr retrieved from the IR camera measurements for cycles 1, 322, and 645 directly before and after occurrence of the crack. Flow direction is top-down.**

10b). Right above cooling channel 4, the temperature is slightly decreased, indicating the beginning of the thinning of the wall between surface and coolant. This effect increases significantly until the last cycle 151 (Fig. 10d). It is caused by the bubble-gum like deformation of the material that starts around cycle 75 (see also Fig. 13a). For CuCrZr the thermal field on the surface remains unchanged for the first half of the test campaign (see Fig. 11a and 11b). For the last cycle (Fig. 11c) the temperature field has become a bit smaller though it has not significantly changed indicating a sudden rupture like it died for Cu-HCP.

3.3 Mechanical Observations

Figures 12, 13 and 14 show the deformation of both TMF panels. Figure 12 presents the development of the displacement of the laser loaded surface obtained with by DIC with the LIMESS system (grey and black lines) for every 5th cycle. The blue line is obtained after the end of the TMF panel test with a Keyence VHX-5000 microscope. The evaluation was executed in the cross-section where the crack occurred. Note that around half of the cycles for Cu-HCP the DIC lost tracking of the speckle marks at the area of highest deformation. It is obvious that both materials deform very different during the course of the test campaign. While Cu-HCP reached a maximum displacement of $\Delta y_{\mathrm{Cu-HCP}} = 0.91$ mm (Fig. 12a), the final displacement of the CuCrZr TMF panel was only $\Delta y_{\mathrm{CuCrZr}} = 0.44$ mm (Fig. 12b).

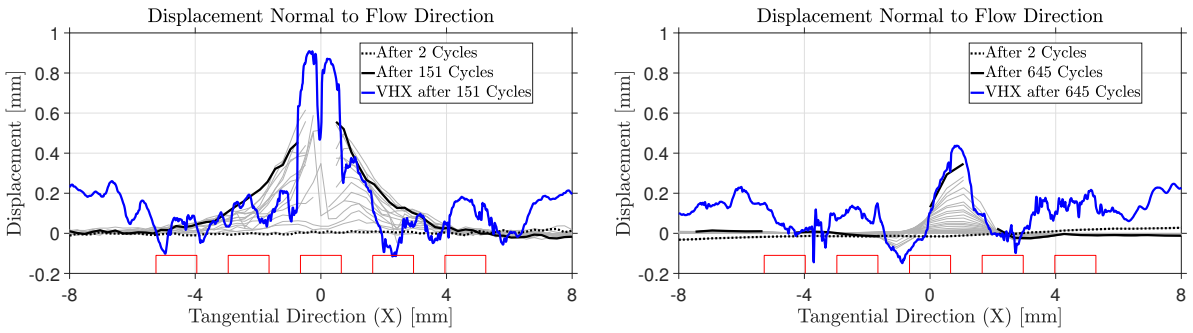

(a) Cu-HCP (b) CuCrZr

Figure 12: **Deformation of the laser loaded surface for every 10th cycle obtained with the LIMESS DIC system (gray, black curves). The blue curve shows the measurement obtained after the test campaign by the VHX-5000. Red lines indicate the position of the cooling channels.**

The respective 3-dimensional plot of the final deformation can be seen in Figure 13. Figure 14 is a CT-Scan of both TMF panels after the test. The CT-Scan also provides insights of the deformation inside the cooling channels.

DOI: 10.13009/EUCASS2023-922

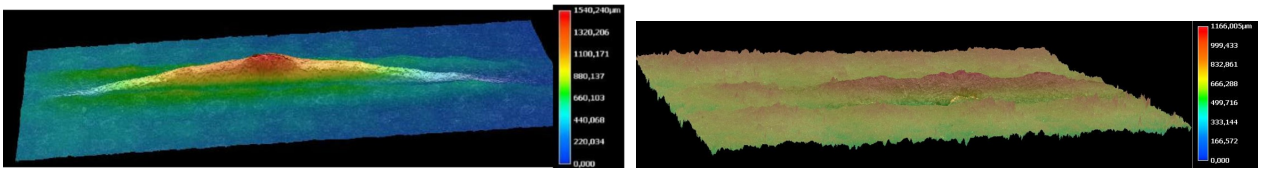

(a) Cu-HCP (b) Cu-HCP

Figure 13: **Elevation plot of the laser loaded surface obtained after the test campaign with the VHX-5000. Flow direction from right to left.**

From Figure 14a it is obvious, that Cu-HCP is a very ductile material at high temperatures, behaving like a bubble-gum. In contrast, CuCrZr in Figure 14b shows a brittle behavior with little deformation. The final size of the elliptically

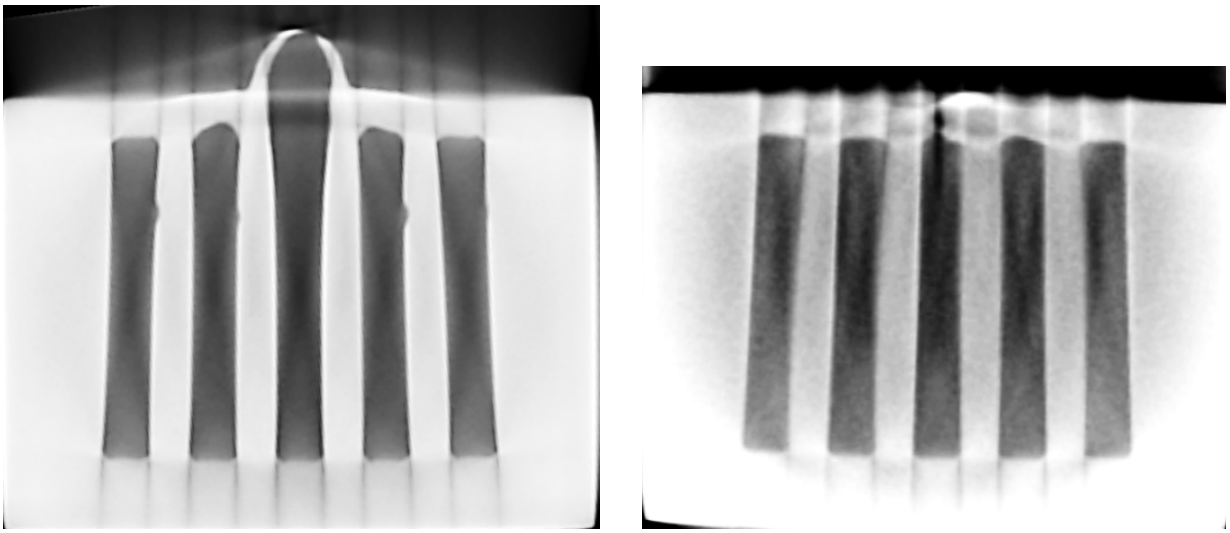

(a) Cu-HCP (b) CuCrZr

Figure 14: **CT-Scan of the TMF panel after the test.**

shaped opening in the Cu-HCP TMF panel is $A_{\mathrm{cr}} = 1.79 \times 0.60\ \mathrm{mm}^2$, for CuCrZr the cracksize at the laser loaded surface of the TMF panel could not be determined as it was too small. The evaluation of the strain in tangential (x) direction on the laser loaded surface obtained by the LIMESS stereo camera system is shown in Figure 15. The plot indicates a linear accumulation of residual strains in case of the Cu-HCP TMF panel 15a for at least the first 61 cycles. Note that after cycle 61 no reasonable results can be delivered by the software any more because the pure copper beneath the coating appears due to high deformation. This causes the software to loose track of the speckle marks applied on the surface. The slope of the fitted tensile strain curve is $\dot{\varepsilon}_{max,fit} = 0.2\%$ while the slope of the fitted compressive strain curve is $\dot{\varepsilon}_{min,fit} = -0.42\%$. Figure 16a shows the spatial distribution of the residual strain after cycle number 60. It can be seen, that tensile strain accumulates above cooling channel 4, while compressive strain accumulates above the fillets next to the central cooling channel. For CuCrZr it seems that in the first 5 cycles a strain of $\varepsilon_{\mathrm{x}} = \pm 0.03$ is developing but being rather constant for almost 360 cycles on that level suggesting some shakedown of the cyclicelasto-plastic deformation (see Fig. 15b). After cycle 360 an exponential development of the tensile strain seems to develop. The same behavior might be interpreted into the curve for compressive strains. However, due to technical difficulties, only a few data points are available. A spatial distribution of the residual strain is also shown in Figure 16b for cycle 279 which is around the same percentage of progress of the test as Figure 16a, hence comparable. Though the strains are much smaller in case of CuCrZr, compressive strains accumulate above the fillets next to the central cooling channel as well and tensile strains accumulate directly above the central cooling channel 4.

4. Summary

The results of the TMF panel tests for Cu-HCP and CuCrZr are presented in this manuscript. The test conditions were $T_{\mathrm{s}} = 800$ K, $\dot{q}_{\mathrm{w}} = 24.25\ \mathrm{MW/m^2}$, $p_{\mathrm{out}} = 55 \pm 0.5$ bar, $T_{\mathrm{in}} = 160 \pm 2$ K. The TMF panel made of Cu-HCP withstood

DOI: 10.13009/EUCASS2023-922

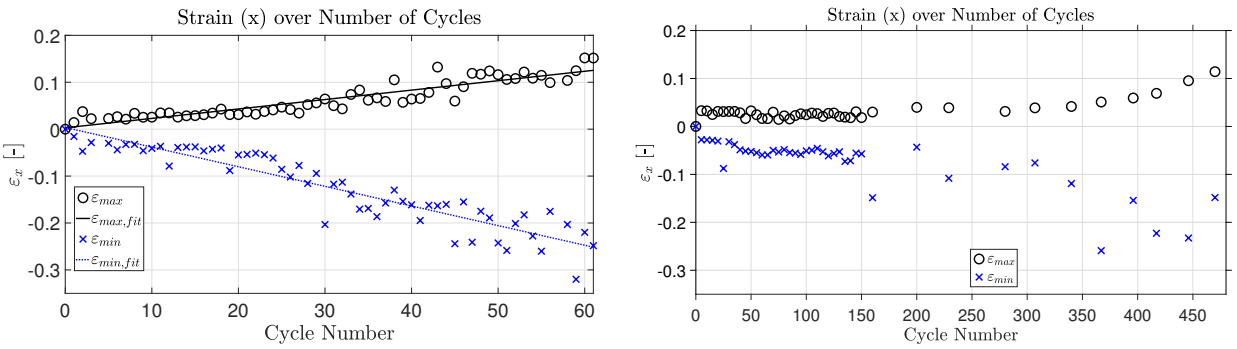

(a) Cu-HCP (b) CuCrZr

Figure 15: **Evolution of locally averaged maximum residual strain over the first 61 cycles as determined with the LIMESS system by DIC.**

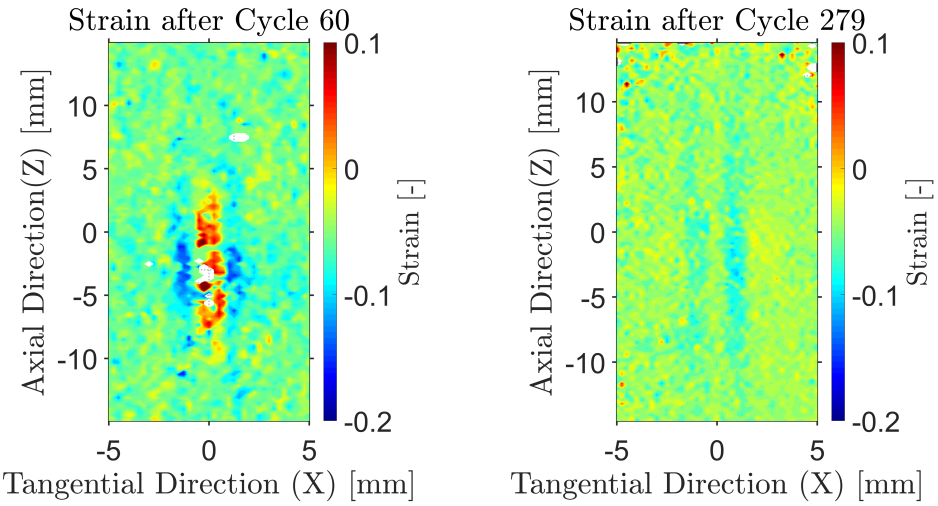

(a) Cu-HCP (b) CuCrZr.

Figure 16: **Exemplary residual strain on the laser loaded surface after around 40% of the overall number of cycles as determined with the LIMESS system by DIC.**

151 laser cycles, the TMF panel made of CuCrZr withstood 645 cycles. Both panels show a very different behavior regarding fluid flow, thermal field and mechanical observations. An important difference is the material performance at high temperatures. Cu-HCP deforms like a bubble-gum, CuCrZr shows a brittle failure. So what do these results imply for rocket engines and in particular reusable liquid rocket engines? First of all, CuCrZr seems to withstand the purely mechanical loading 4.3× longer than Cu-HCP does. Furthermore, the high bubble-gum-like deformation of Cu-HCP will likely cause high turbulence at the inner combustion chamber wall leading to an even higher temperature downstream, the comparably small deformation of CuCrZr will cause less turbulence. Again, note that only the mechanical performance was evaluated here, leaving the resistance against effects like abrasion, blanching etc out of consideration. Summarizing that, CuCrZr seems to be better suitable for reusable liquid rocket engines. However, Cu-HCP can be used for expendable upper stages due to its extremely high heat conductivity, availability and low price.

5. Acknowledgments

The authors thank the European Space Agency (ESA) for funding and Dr. Gordan Thiede for his work at the early stages of the project. Furthermore the authors would like to express their gratitude to Prof. Dr.-Ing. Thomas Seifert, Hochschule Offenbach, and Dr. Christoph Schweizer, Fraunhofer IWM Freiburg, for determination of the material parameters. Also the authors thank Mr. Ralf Lichtenberger of LIMESS GmbH for his extensive support with the DIC and Raouf Jemmali (DLR) for conducting the CT-Scan as well as Sebastian Kahl for maintaining and operating the TMF test bench.

DOI: 10.13009/EUCASS2023-922

References

[1] Shaista Babar and J. H. Weaver. Optical constants of cu, ag, and au revisited. *Applied Optics*, 54(3):477, jan 2015.

[2] A. Carden, D. Harman, and E. Franco-Ferreira. Thermal fatigue analysis of a cryogenically cooled rocket nozzle. Technical report, Oak Ridge National Labaratory, Oak Ridge, Tennessee, 1966.

[3] Andreas Gernoth. *Untersuchung der Turbulenzmodellierung von rauen Rechteckkanalströmungen mit Berücksichtigung der Oberflächenverformung im Hinblick auf die Anwendung in Raketenmotoren*. PhD thesis, Universität Stuttgart, 2013.

[4] Andreas Gernoth, Jörg R. Riccius, Oskar Haidn, Ludwig Brummer, Bernd Mewes, and Katharina Quering. Tmf panel tests: close-to-reality simulation of thermo-mechanical fatigue processes in heat-loaded walls. In *44th AIAA/ASME/SAE/ASEE Joint Propulsion Conference & Exhibit*, Juli 2008.

[5] Felix Hötte, Christoph v. Sethe, Torben Fiedler, Matthias C. Haupt, Oskar J. Haidn, and Michael Rohdenburg. Experimental lifetime study of regeneratively cooled rocket chamber walls. *International Journal of Fatigue*, 138:105649, sep 2020.

[6] Pascal H. Kringe, Chris Burger, Jörg R. Riccius, Evgeny Zametaev, Michael Oschwald, Andreas Gernoth, Sebastian Soller, Marcus Lehmann, and Stefanie Reese. Dependency of surface temperature on coolant mass flow and heat flux in rocket combustion chambers. In *2022 IEEE Aerospace Conference (AERO)*. IEEE, mar 2022.

[7] Pascal H. Kringe, Jörg R. Riccius, Justin Hardi, Michael Oschwald, Andreas Gernoth, Sebastian Soller, Marcus Lehmann, and Stefanie Reese. Experimental and numerical fatigue life study of inner liner material in rocket combustion chambers. In *2023 IEEE Aerospace Conference*. IEEE, mar 2023.

[8] Pascal H. Kringe, Jörg R. Riccius, and Michael Oschwald. Low-cost life assessment of liquid rocket engines by replacing full-scale engine tests with tmf panel tests. *Journal of the British Interplanetary Society*, 73(5):152 –162, May 2020.

[9] Pascal H. Kringe, Jörg R. Riccius, Evgeny Zametaev, Michael Oschwald, Andreas Gernoth, Sebastian Soller, Marcus Lehmann, and Stefanie Reese. Dependency of inner liner surface temperature on coolant mass flow rate and heat flux in rocket combustion chambers. In *Space Propulsion 2020 + 1*, 2021.

[10] Michael Oschwald, Dmitry Suslov, and Alexander Woschnak. Temperature dependence of material properties and its influence on the thermal distribution in regenratively cooled combustion chamber walls. In *1st EUCASS*, 2005.

[11] R. J. Quentmeyer. Experimental fatigue life investigation of cylindrical thrust chambers. In *13th Propulsion Conference*. American Institute of Aeronautics and Astronautics, jul 1977.

[12] Jörg R. Riccius, Micha W. Böttcher, and Hugo Duval. A first step into the blanching modelling of liquid rocket engines: taking into account the roughness increase of the chamber wall. 2019.

[13] Jörg R. Riccius, Andreas Gernoth, Elena Suslova, Christian Böhm, Evgeny Zametaev, Oskar Haidn, Ludwig Brummer, Bernd Mewes, Oliver Knab, Michael Terhardt, and Gerald Hagemann. Tmf: Laser application for a close-to-reality simulation of thermo-mechanical fatigue processes in rocket engines. In von Karman Institute and ULB, editors, *EUCASS 2007*, Juli 2007.

[14] Thomas Seifert and Christoph Schweizer. Material characterisation test report for temperatures above 273 k. Technical Report (ESA AO 1-8445/15/NL/LVH), Offenburg University of Applied Sciences and Fraunhofer IWM, in: Cyclic Thermomechanical Loading of Actively Cooled Wall Structures, CLAWS D4 Report, 2019.

[15] Dmitry Suslov, Alexander Woschnak, Dirk Greuel, and Michael Oschwald. Measurement techniques for investigation of heat transfer processes at european research and technology test facility p8. In *1st EUCASS*, 2005.

[16] Gordan Thiede. *Validation of Damage Parameter Based Finite Element Fatigue Life Analysis Results to Combustion Chamber Type Thermomechanical Fatigue Panel Tests*. PhD thesis, Rheinisch-Westfälische Technische Hochschule Aachen, 2019.

DOI: 10.13009/EUCASS2023-922

[17] Gordan Thiede, Jörg R. Riccius, and Stefanie Reese. Life prediction of rocket combustion-chamber-type thermo-mechanical fatigue panels. *Journal of Propulsion and Power*, Juli 2017.

[18] Wolfgang S. M. Werner, Kathrin Glantschnig, and Claudia Ambrosch-Draxl. Optical constants and inelastic electron-scattering data for 17 elemental metals. *Journal of Physical and Chemical Reference Data*, 38(4):1013–1092, dec 2009.